J. Fluid Mech. (2002), *vol.* 463000, *pp.* 377–402.
DOI: 10.1017/S002211200200890X Printed in the United Kingdom

Multiple-arrayed pressure measurement for investigation of the unsteady flow structure of a reattaching shear layer

By INWON LEE† AND HYUNG JIN SUNG

Department of Mechanical Engineering, Korea Advanced Institute of Science and Technology, 373-1, Kusong-dong, Yusong-ku, Taejon, 305-701, Korea

(Received 9 May 2001 and in revised form 8 February 2002)

Spatio-temporal characteristics of wall pressure fluctuations in separated and reattaching flows over a backward-facing step were investigated through an extensive pressure-velocity joint measurement with an array of microphones. The experiment was performed in a wind tunnel with a Reynolds number of 33 000 based on the step height and the free-stream velocity. Synchronized wavelet maps showed the evolutionary behaviour of pressure fluctuations and gave further insight into the modulated nature of large-scale vortical structures. To see the relationship between the flow field and the relevant spatial mode of the pressure field, a new kind of wavenumber filtering, termed 'spatial box filtering' (SBF), was introduced and examined. The vortical flow field was reconstructed using every single-point velocity measurement by means of the conditional average based on the SBF second mode of pressure fluctuations. The flow field showed a well-organized spanwise vortical structure convected with a speed of $0.6U_0$ and a characteristic 'sawtooth' pattern of the unsteady trace of reattachment length. In addition to the coherent vortical structures, the periodic enlargement/shrinkage process of the recirculation region owing to flapping motion was analysed. The recirculation region was found to undergo an enlargement/shrinkage cycle in accordance with the lowpass-filtered component of pressure fluctuations. In addition, such modulatory behaviour of the vortical structure as the global oscillation phase was discussed in connection with the conditionally averaged flow field.

1. Introduction

The understanding of flow structure in turbulent shear flows with separation and reattachment is of immense importance in design and control aspects of many engineering applications, such as aerodynamic performance of airfoil with separation, wind loading of structures, overall efficiency of combustors. The unsteady coherent structure of separated and reattaching flow over a backward-facing step is the current subject of a large number of experimental and numerical studies. A comprehensive review of the experimental investigations associated with the time-mean characteristics of this flow regime is given in Eaton & Johnston (1981).

A literature survey reveals that many studies have been performed to find an intrinsic unsteady feature in separated and reattaching flows (Eaton & Johnston 1982; Cherry, Hillier & Latour 1984; Kiya & Sasaki 1985; Driver, Seegmiller &

† Present address: Digital Appliance Research Laboratory, LG Electronics, 327-23, Gasan-dong, Geumchun-gu, Seoul, 153-802, Korea.

Marvin 1987; Heenan & Morrison 1998). Two kinds of unsteadiness have been demonstrated; one is large-scale vortices and the other is flapping. It is known that the flapping frequencies are about six or eight times smaller than those associated with the large-scale vortices. Eaton & Johnston (1982) attributed the cause of flapping to an instantaneous imbalance between entrainment of fluid from the recirculation region and that rejected from near reattachment. Cherry *et al.* (1984) demonstrated the modulation of large-scale vortex shedding in accordance with the flapping phase. They further suggested that the flapping was indicative of a growth–decay cycle of the separation bubble. According to Kiya & Sasaki (1985), the flapping was caused by the inflation of the separation bubble owing to a reduced entrainment rate by the mixing layer from the separation bubble, which results from a short-term breakdown in the spanwise coherence of the shear layer. This instantaneous inflation of the separation bubble is then accompanied by the subsequent sudden release of fluid, thereby completing a feedback mechanism. This reasoning, based on the mass imbalance, seems to be qualitatively effective in the sense that Heenan & Morrison (1998) successfully attenuated the flapping motion by placing a porous plenum beneath the recirculating region, thereby absorbing the mass efflux due to the instantaneous mass imbalance.

For feedback control of general reattaching shear flows, it is necessary to capture the above unsteadinesses and to predict the entire flow structure as quickly as possible with finite instrumentation capacity. The feasible on-line detection method for the coherent structures is to use the information of pressure fluctuations, as shown by Kiya & Sasaki (1985). Other methods such as flow visualizations are basically qualitative and off-line. Since the pressure fluctuations in the incompressible flows are governed by the Poisson equation with the velocity gradient source term, the pressure fluctuations in one point are a weighted sum of every contribution of the whole flow field. Moreover, the measurement of surface pressure fluctuations is intrinsically non-intrusive and easily expandable to a multi-sensor application, where the spatio-temporal flow information is obtainable.

The application of an array of pressure sensors has been dealt with in Lee & Sung (2001*a*) and Lee & Sung (2001*b*) (hereinafter referred to as LS1 and LS2, respectively). In these studies, new dynamical aspects of pressure fluctuations were found and shown to be closely related to the relevant coherent structures. However, joint measurements of velocity and pressure fluctuations should be performed to establish a direct and more detailed relationship between the flow physics and the spatio-temporal modes of pressure fluctuations. This kind of joint measurement has been a popular study for various flow fields (Hijikata, Suzuki & Iwana 1996; Johansson, Her & Haritonidis 1987). However, the conventional single-point measurement of pressure as the conditioning signal for the velocity field measurement might be influenced by localized small-scale events so that a smearing phenomenon of the results may occur. This was pointed out by Cherry *et al.* (1984) who noted that: '*the large-scale shear-layer structures do not necessarily appear to be, on average, responsible for particularly large-amplitude pressure fluctuations.*' Furthermore, different spatial modes such as global oscillation and vortex convection, which were found in LS2, could appear to be similar from a single-point measurement. Kiya & Sasaki (1985) suggested that the employment of multiple pressure fluctuations acquired from suitably arranged positions as conditioning signals could be a promising method. Thus, the velocity field measurement based on multi-point pressure information can be made immune to the irrelevant mode contributions. In addition, detailed flow structures related to specific spatial modes of pressure fluctuations can be provided.

The main objective of the present study is to identify large-scale structures with the spatial information of surface pressure fluctuations. The spatial signal processing can provide an on-line diagnosis of the flow for the feedback control. Toward this end, in the present study, every velocity time history at a total of 777 points (37×21 points in the x- and y-directions, respectively) was measured simultaneously with the spatio-temporal distributions of pressure fluctuations from a 29-sensor array of microphones. The pressure data as a function of both space and time are to be processed in an adequate manner to extract a meaningful flow structure from the measured velocity data. In addition, a novel on-line pressure data processing method, termed here 'spatial box filtering', will be introduced and discussed. A conditionally averaged velocity vector field as well as dynamic features of the recirculation region will be obtained based on the pressure signal processing method. The composition of this study is as follows. In § 2, the experimental apparatus will be presented. The preliminary results from pressure-alone measurement in LS1 and LS2 will be discussed in § 3. In § 4, the signal processing method of the joint pressure–velocity measurement and the results of the large-scale vortical structures will be shown. The flapping motion will be discussed in terms of the conditionally averaged streamfunction in § 5. Finally, the summary of results will be given in § 6.

2. Experimental apparatus

2.1. *Wind tunnel and test section*

A subsonic open-circuit wind tunnel (Chun & Sung 1996), was slightly modified for the present experiment. A more detailed explanation regarding the wind tunnel can be found in LS1. The dimensions of the inlet channel were 630 mm in width, 100 mm in height and 1000 mm in length. The free-stream turbulence intensity which was measured on the centreline of the inlet channel at 100 mm upstream of the channel exit was less than 0.6% at speeds of 5–25 m s^{-1}. No significant peaks were found in the spectrum of velocity fluctuations in the main flow. The step edge was attached to the end of the inlet channel, which was 1000 mm downstream of the trip wire at the entrance of the inlet channel. At this location, a constant-area rectangular duct, whose dimensions were 630 mm in width, 150 mm in height, and 2500 mm in length, was constructed to act as the backward-facing step. The step height H of the backward-facing step was 50 mm and the aspect ratio $AR = 12.5$. For the present experimental rig, a two-dimensional-flow assumption is applicable to a reasonable accuracy, at least for much of the central portion of the test section. An AR ratio greater than 10 has been recommended by de Brederode & Bradshaw (1978) to avoid significant sidewall effects in the vicinity of the centreline of the channel. Therefore, the flow is assumed to maintain two-dimensionality along the centreline of the test section.

2.2. *32-channel pressure-alone measurement set-up*

In the present study, an Acousticel array microphone system (The Modal Shop Inc., model TMS130A) was used for sensing the pressure fluctuations. This system consists of 32 electret condenser microphones, with a diameter of 10.54 mm and a height of 25.4 mm, connection cables and a 32-channel differential amplifier (Model 514A). The sensitivity and frequency response of each microphone was measured by comparison with a half-inch reference microphone (B & K type 4133), which was installed together with the Acousticels in an acoustic array calibrator (model 9080C). The details concerning the calibration procedure are given in LS1, and the calibration

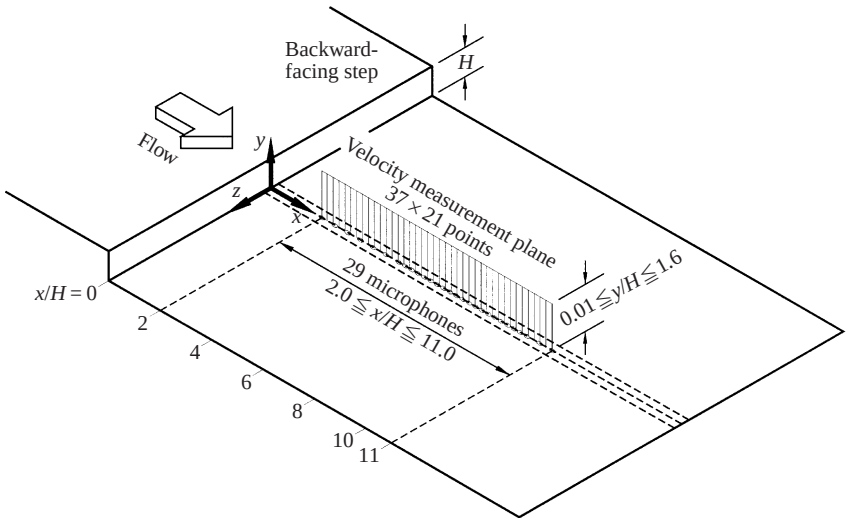

FIGURE 1. Schematic diagram of the test section.

results indicated that the magnitude error and the phase delay were below ± 1 dB and $\pm 3^{\circ}$, respectively, in the frequency range of 5–10 kHz. This 'flat' response, together with the wide dynamic range of 42–142 dB, guarantees high levels of measurement accuracy without any further compensation procedure of the Acousticel output.

Figure 1 illustrates the installation methods of the microphone array in the test section. A 5 mm thick aluminium plate was inserted into a slot machined along the centreline of the section. On each side of the aluminium plate, 1 mm diameter pressure measuring holes and a 10.6 mm diameter microphone installation hole were placed concentrically. The Helmholtz resonance frequency from the present apparatus was estimated to be 3750 Hz. The origin of the coordinate system is located on the midpoint of the most upstream edge of the bottom wall. The interval between each Acousticel $\Delta\xi_0$ was set as 12.5 mm, giving $\Delta\xi_0/H = 0.25$. Thus, the 32 Acousticel array spans a streamwise extent of $7.75H$. For one set of measurement, 32 pressure–time histories were acquired with the effective sampling frequency of 1953.125 Hz using a 32-channel A/D converter DT2839 (Data Translation Inc.). The acoustic contamination by fan noise is important to ascertain the reliability and accuracy of the present experiment. Toward this end, the spectrum of the fan noise is plotted in figure 2, in comparison with the pressure spectra at various streamwise locations. The noise spectrum was measured at the entrance of the test section. As seen in figure 2, the pressure spectra are much higher than the noise spectrum by at least 20 dB. The major low-frequency component below 100 Hz is not affected by the fan noise. Furthermore, the present 'spatial box filter' is a high-wavenumber spatial filter whose wavelength is far shorter than the wavelength of the sound in the frequency range below 100 Hz. Accordingly, the sound contamination is negligible in the present study.

Apart from the pressure measurement, the usual hot-wire technique was used, together with a constant-temperature anemometer (TSI-IFA300) for the measurement of the mean velocity field and time-mean reattachment length x_R. A split-film probe (TSI model 1288) was used to measure the fluctuating velocity statistics and the forward-flow time fraction γ_p. An improved version of the calibration method was carefully employed to obtain more reliable and accurate calibration data (Ra, Chang

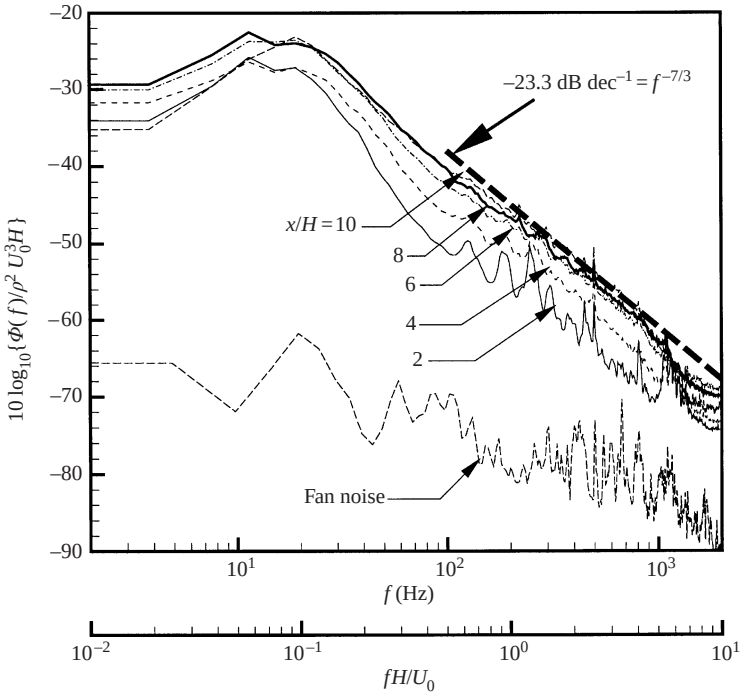

FIGURE 2. Spectra of pressure at various streamwise locations and spectrum of fan noise.

& Park 1990). The forward-flow time fraction γ_p was defined as the time fraction of downstream flow and was further used in estimating the reattachment length x_R (Chun & Sung 1996). A total of 204 800 voltage samples at each position were averaged and sent to a Pentium PC after the velocity signals were digitized by means of a 4-channel A/D converter (UEI WIN-30DS). All these instruments were remotely controlled using an in-house LabVIEW program.

2.3. *Pressure–velocity joint measurement set-up*

In this measurement set-up, the array of 29 Acousticel microphones was located along the centreline of the test section. As shown in figure 1, the array was set up with a non-uniform interval so that it spanned a streamwise extent of $9H$ from $x/H = 2.0$ to $x/H = 11.0$. This was to certify a wider spatial extent $2.0 \leqslant x/H \leqslant 11.0$, where most of the separated and reattaching flow took place, with a single array consisting of a limited number of microphones. The interval between each microphone was set at $0.25H$ for the reattaching region $5.0 \leqslant x/H \leqslant 10.0$, whereas it was $0.5H$ for the other regions. As seen in figure 1, velocity time history was measured on an (x, y) centreplane of the test section. The velocity measurement grid of 37×21 extended over $2.0 \leqslant x/H \leqslant 11.0$ and $0.01 \leqslant y/H \leqslant 1.6$. Note that $y/H = 0.0$ refers to the bottom wall of the step owing to the coordinate system defined in figure 1. Grid spacing in the x-direction was uniform ($\Delta x = 0.25H$), whereas a stretched grid was used in the y-direction with fine spacings near the bottom wall. The hot-wire technique was used to measure u- and v-velocity. Since the split-film probe (TSI model 1288), whose split plane is aligned with the transverse y-direction, cannot predict the polarity of the v-velocity, this probe was employed only for the measurement of u-velocity. Instead,

for the measurement of v-velocity, another split-film probe (TSI model 1287) with the split plane being parallel to the streamwise direction was used.

For every velocity time history measurement, pressure–time history from a total of 29 microphones were simultaneously acquired using the 32-channel A/D converter DT2839 (Data Translation Inc.) with an effective sampling frequency of 488.28125 Hz. Originally, all data had been oversampled 4 times with a sampling frequency of 1953.125 Hz and one of every four pressure readings was then recorded in order to reduce the interchannel sampling delay. Since the original sampling frequency was high enough to neglect the high-frequency pressure components, anti-aliasing was not required. Instead, a digital lowpass filter was employed before taking one data point out of every 4 samples. Each pressure– or velocity–time history contained 163 840 data points, and they were stored in a Pentium PC for further data processing. As will be discussed in § 4 and § 5, the extensive amount of spatio-temporal pressure data enables a comparative examination of various signal-conditioning methods for the prediction of large-scale structure. In this manner, an appropriate spatial mode of the pressure fluctuations could be found toward the extraction and reconstruction of a meaningful flow structure from the combination of the conditional average of every single velocity–time history. Regarding the probe interference with microphones, it was found that the r.m.s. and the spectra of pressure are very slightly increased by the disturbance of the split film. The number of conditional averages without the split film was decreased by 1.5%, which was negligible. An uncertainty analysis of the data suggested that the u- and v-velocity components were measured within $\pm 5\%$ throughout the recirculation region. The uncertainty in the pressure measurement was estimated to be $\pm 3\%$ throughout the whole array of microphones. These uncertainties in the velocity and pressure measurement are presented in figures 6 and 8, respectively.

3. Results from pressure-alone measurement

3.1. *Spatio-temporal features of pressure fluctuations*

In the present experiment, the Reynolds number based on the step height $Re_H = 33\,000$ is selected, which is the same as in the experiment of Chun & Sung (1996). When rescaled by the momentum thickness, this corresponds to $Re_\theta = 1300$. Among the various data representing the backward-facing step flow, the reattachment length x_R is frequently used as a representative quantity in a time-mean sense. In order to find the reattachment length, the forward-flow time fraction γ_p in the vicinity of the wall ($y/H = 0.02$) is measured by using a split-film probe (TSI model 1288). The time-mean reattachment position x_R can be defined as the point where the forward-flow time fraction has the value $\gamma_p = 0.5$. The reattachment length is found to be $x_R = 7.4H$. Details regarding the mean and fluctuating velocity profiles and other quantities can be found in Chun & Sung (1996). Before proceeding further, it would be advantageous to look into the space–time characteristics of wall pressure fluctuations. Figure 3 exhibits the space–time contour plots of instantaneous wall pressure fluctuations, normalized by the free-stream dynamic pressure $q = 1/2\rho U_0^2$, measured for $2.0 \leqslant x/H \leqslant 9.75$. Note that this figure consists of two 'time slides' with figure 3(a) preceding figure 3(b). The downstream convective feature, denoted by an inclined contour pattern, is observed in both figures. The upstream convection is scarcely found, which is consistent with the positive convection velocity estimation of $0.6U_0$ in LS1. It is well known that the instantaneous negative peaks in wall pressure fluctuations are associated with the passage of large-scale vortices (Cherry *et al.* 1984;

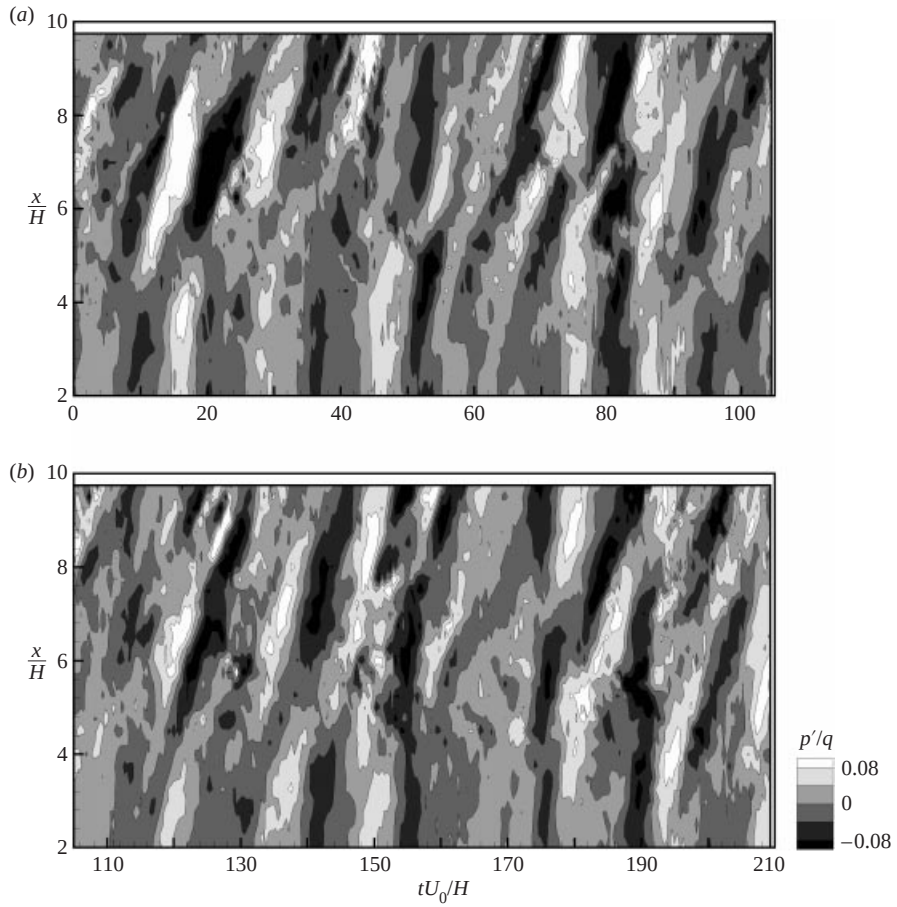

FIGURE 3. Space–time contour plots of pressure fluctuations.

Kiya & Sasaki 1985). Also, the positive peaks are induced by the downward inrush of free stream between vortices. A closer inspection of figure 3 reveals that the pressure fluctuations are globally in phase and oscillate as a whole at some time instances, i.e. $tU_0/H \sim 80$ and 190. In addition, the pressure fluctuations are more intensive at this 'global oscillation' phase. Between the global oscillation phases, the convection of vortices seems to be prevailing. However, the strength and the spatial extent of each vortex are not uniform. Namely, relatively small-scale behaviours are dominant at $tU_0/H \sim 50$.

3.2. *Wavelet transform analysis*

As mentioned in LS1, the streamwise wavenumber spectra together with the above-stated space–time cross-correlation indicated the existence of a stationary mode and the scale variations of shed vortices. To scrutinize the modulated spatio-temporal behaviour, a time-dependent analysis based on the wavelet transform is employed in this study. The wavelet transform $W(a,b)$ of a continuous real-valued time signal $x(t)$ is defined as the inner product between $x(t)$ and the analysing wavelet $\psi_{a,b}(t) = (1/\sqrt{a})\psi((t-b)/a)$ (Farge 1992). Here, a is the timescale dilation parameter and b is the time translation parameter. A more detailed explanation concerning the mathematical definitions can be found in LS2. Among the various wavelets proposed

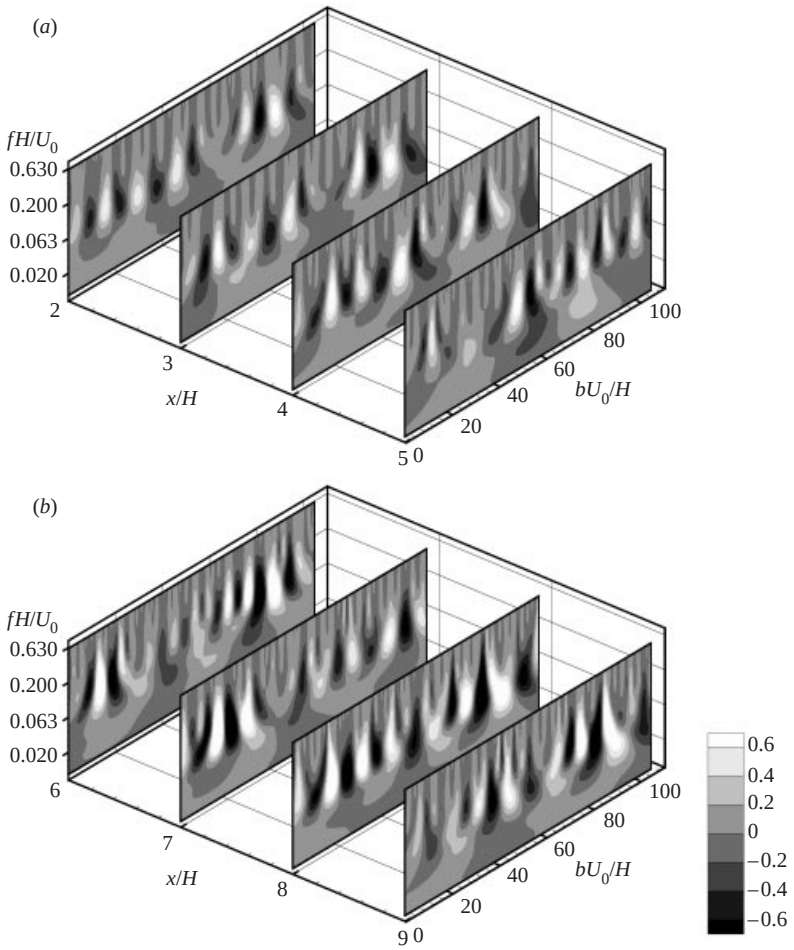

FIGURE 4. Contour plots of wavelet transform. (*a*) $2.0 \leqslant x/H \leqslant 5.0$; (*b*) $6.0 \leqslant x/H \leqslant 9.0$.

so far, consideration is given to a real-valued 'Mexican hat' wavelet, which is defined as $\psi(t) = (1 - t^2)\exp(-\frac{1}{2}t^2)$. This wavelet is known to be effective in resolving high-amplitude peaks in the signal (Addison 1999; Poggie & Smits 1997). Compared to the Morlet wavelet, the Mexican hat wavelet provides better temporal resolution at the expense of frequency resolution.

Figure 4 shows the contour plots of wavelet transform, calculated at eight locations from the array with $X_0 = 2.0$ ($2.0 \leqslant x/H \leqslant 9.75$) with the interval H. A non-dimensional frequency fH/U_0 is employed on the z-axis. As mentioned earlier, it is noteworthy that every plot of $W(a, b)$ has been synchronized because the pressure–time histories from all points in the array are simultaneously acquired. Thus, the spatially evolving characteristics of various frequency components can be displayed. The regular extrema along the frequency $fH/U_0 \sim 0.063$ correspond to the frequency of large-scale vortices, which was shown to be $fH/U_0 \sim 0.065$ in LS1. It can be seen that this vortical component contains most of the energy of the pressure fluctuations. This suggests that the shed vortices are largely responsible for the pressure fluctuations. The increase of r.m.s. pressure along the streamwise direction can be identified by simply comparing the maxima and minima of the wavelet

transform at various locations. A perusal of individual contour plots discloses that the large-scale vortical mode of pressure fluctuations undergoes energetic and quiescent phases. This tendency is evident in the forward part of the recirculation region (figure 4*a*).

In the reattaching region ($x/H = 8.0$ in figure 4*b*), the small-scale components are discernible near $bU_0/H \sim 50$. A closer inspection of figures 3 and 4(*b*) indicates that the appearance of small-scale components is correlated with the initial stage of the vortex convection phase. At this stage, the separate extrema with low and high frequencies demonstrate the breakdown of large-scale vortices. On the other hand, the contour plot exhibits simpler patterns in other stages. It seems that the frequency composition of eddies is influenced by the phase of flapping motion. Further downstream at $x/H = 9.0$, the small-scale disturbances decay out and a new regular pattern is re-established. Eaton & Johnston (1981) reported the controversy between two models concerning the reattachment process: the downstream-moving small eddies, in contrast to the eddies moving alternately upstream and downstream. The upstream convection has not been observed in the present wavelet transform analysis, which is consistent with the result in LS1. Furthermore, the breakdown of eddies has not been observed at every large-scale vortical structure. Since the pressure fluctuations at a given point are in principle influenced by velocity fluctuations in the neighbouring region of the flow, it seems to be inadequate to investigate the behaviour of small-scale eddies from the wavelet transform of pressure fluctuations. Nevertheless, it is obvious that the reattachment process gives rise to a multitude of events with different frequency compositions, rather than a unique predetermined one.

Since the wavelet transform is performed at each pressure–time history, it may be possible to define the wavelet transform in a three-dimensional space (x, b, f). Accordingly, the isosurface of large magnitude of the wavelet transform, whose planform view is given in figure 5(*a*), represents a locus of high energy in the pressure fluctuations in space and time. The values of 0.6 and -0.6, approximately 40% of the maximum magnitude, have been chosen arbitrarily to define the isosurfaces. The alternating occurrences of the global oscillation phase and the vortex convection phase are clearly seen in figure 5(*a*). Figure 5(*b*) is a cross-sectional contour plot of the wavelet transform at $fH/U_0 = 0.06458$, where the space–time variation of wavelet transform is most energetic. Note that the frequency corresponding to the most energetic scale coincides with the frequency of large-scale vortices ($fH/U_0 \sim 0.065$). At the beginning of the vortex convection phase near $bU_0/H \sim 100$, the inclined contours branch off from the vertical contours near $x/H = 4.0$. In addition, the end of the vortex convection phase is marked by a merging of the inclined contours back into the stationary vertical contours at $bU_0/H \sim 185$. These sequential phenomena can be described by the following scenario for the large-scale vortices: first, a global intense oscillation appears with the contraction of the separation bubble. As the bubble enlarges, the separated shear layer receives positive momentum in the streamwise direction. After a quiescent period, a large-scale vortical structure emerges and is then accelerated to form an orderly structure behind it. Secondly, these periodic vortices convect downstream. Finally, the vortices are decelerated and the next global oscillation redevelops.

For the validation of this scenario, a prerequisite is the presence of periodic enlargement and shrinkage of the recirculation region with very low frequency. This was identified by Kiya & Sasaki (1985) in a separation bubble flow. In the motion of a lowpass-filtered instantaneous reattachment point, the enlargement and shrinkage

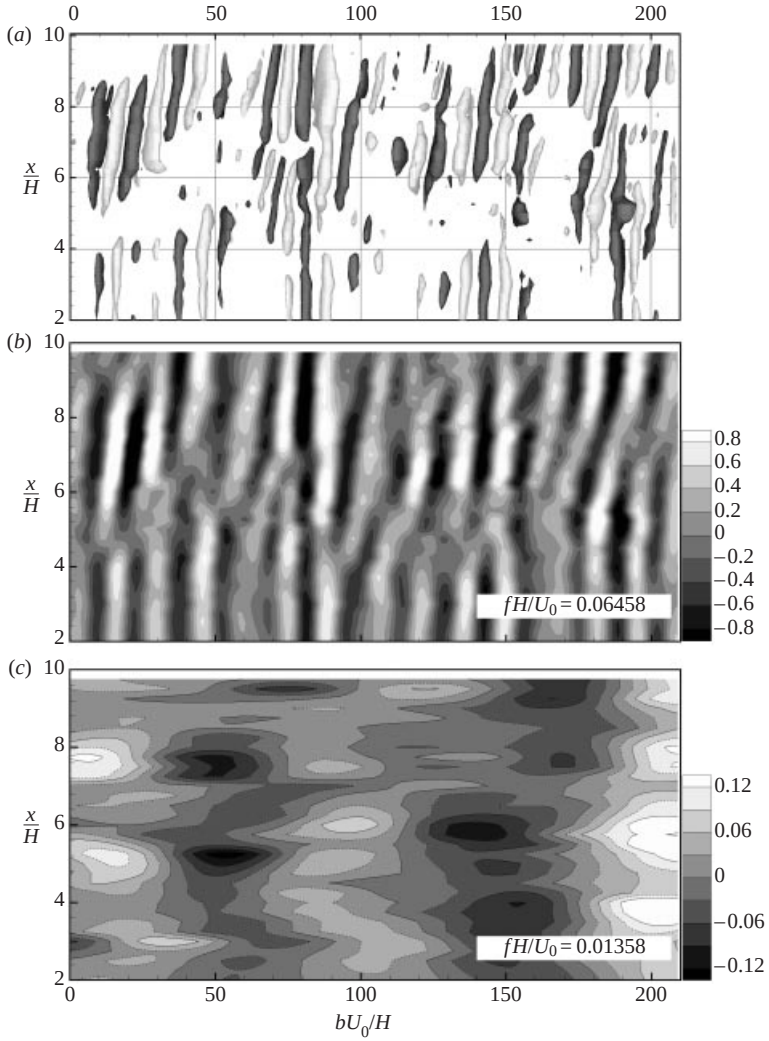

FIGURE 5. Planform views of wavelet transform. (*a*) Isosurfaces. (*b*) Contour plot at $fH/U_0 = 0.06458$. (*c*) Contour plot at $fH/U_0 = 0.01358$.

of a separation bubble were observed in connection with the peak and valley of the lowpass-filtered pressure fluctuations p_F measured at the time-mean reattachment point. To be more specific, the enlargement of the separation bubble is associated with the positive value of p_F and vice versa. This is analogous to a simple model in which the separation bubble is regarded as a periodically inflating sphere. Eaton & Johnston (1982) also reported the existence of the flapping motion, whose frequency is below $fH/U_0 = 0.02$ in a flow over a backward-facing step.

Kiya & Sasaki (1985) suggested that the pressure fluctuations associated with the flapping motion can be approximated by a standing wave. A standing wave of very low frequency is indeed found in the present study; figure 5(*c*) is another cross-sectional contour plot at the flapping frequency $fH/U_0 = 0.01358$. The flapping frequency component in figure 5(*c*) can be considered to demonstrate standing wave characteristics. This frequency component of the pressure fluctuations is referred to as p_F hereinafter. The time relation between the afore-stated shedding modes and the

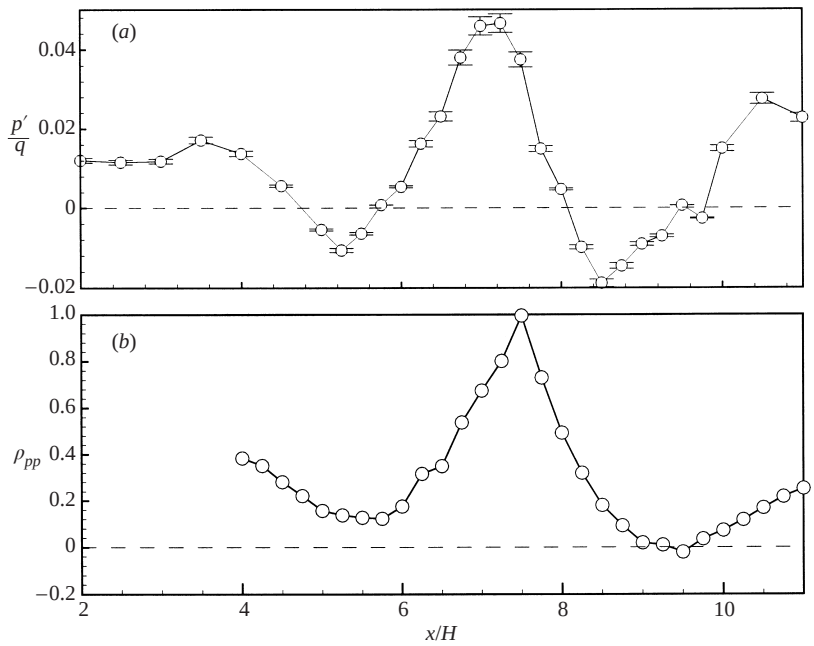

FIGURE 6. Streamwise scale of pressure fluctuations. (*a*) Streamwise distribution of the conditionally averaged pressure fluctuations. (*b*) Cross-correlation coefficient of pressure fluctuations $\rho_{pp}(x, \tau = 0)$ with the origin $X_0/H = 7.5$.

flapping phase can be detected by comparing figures 5(*b*) and 5(*c*). It is seen that the global oscillation phase coincides with the increasing zero of p_F ($p_F = 0$, $\partial p_F/\partial t > 0$). In the following sections, a deeper and closer examination of this observed result will be given in terms of the results from the joint pressure–velocity measurement.

4. Features of the large-scale vortical structure

4.1. *Spatial mode of pressure: spatial box filtering*

As indicated in § 1, the main objective of the present study is to investigate flow structure based on the spatio-temporal distribution of pressure fluctuations. The feasibility of extracting a meaningful flow pattern by means of a conditional average of velocity–time history based on the pressure information is concerned. The advantage of a multi-point measurement as a conditioning signal was suggested in § 1, i.e. the immunity to irrelevant small-scale mode contributions. In this study, the attention has been focused on the use of instantaneous spatial distribution of pressure fluctuations with time. This enables an on-line prediction of the flow structure associated with a specific spatial mode of pressure fluctuations and could be further applied to the feedback control of reattaching flows.

Toward this end, a relevant spatial scale of the pressure fluctuations is required. In figure 6(*a*), the streamwise distribution of conditionally averaged pressure fluctuations, normalized by the inflow dynamic pressure ($\frac{1}{2}\rho U_0^2$), is displayed. This is an average of the instantaneous pressure distribution when the transverse velocity fluctuations v' at $(x, y) = (7.5H, 1.0H)$ exceed $-2.5v_{rms}$. There exists a negative correlation between the pressure and v'. The pressure peak associated with the excursion of transverse velocity is of the order of $1.5p_{rms}$. The spatial distribution, where the main peak is

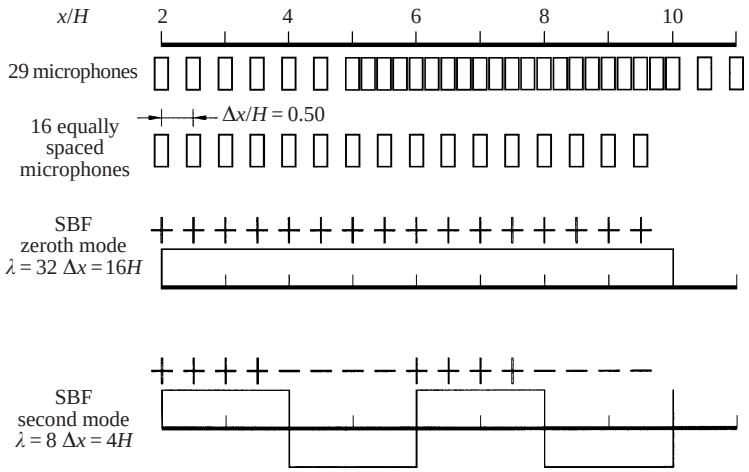

FIGURE 7. Schematic diagram of spatial box filtering.

surrounded by the negative upstream and downstream valleys, is attributable to the spatial periodicity of the large-scale vortical structure. In figure 11 of Kiya & Sasaki (1985), where the time history of pressure fluctuations at the reattachment point was conditionally averaged, the positive pressure fluctuations were shown to coincide with the inrush of the outer irrotational fluid with high total pressure towards the wall. The negative excursion of the transverse velocity in figure 6(*a*) was intentionally set to meet this inrush. The similarity between the waveforms of Kiya & Sasaki (1985) and the present results suggests that the present conditional average is closely related to the large-scale vortical structure. In addition, a similar result was observed by Cherry *et al.* (1984). Figure 6(*b*) represents the cross-correlation coefficient of pressure fluctuations $\rho_{pp}(x, \tau; X_0)$ with zero time delay at $X_0/H = 7.5$. In both figures 6(*a*) and 6(*b*), the spacing between the two valleys is approximately $4H$, which is the spacing between large-scale vortices. This spacing corresponds to $0.54x_R$, which is close to the $0.6x_R$ reported by Kiya & Sasaki (1985).

From this observation, the spatial mode of pressure fluctuations associated with the large-scale vortical structure attains a streamwise scale of $4H$. Accordingly, the main concern is placed on the correlation between the above length scale and the coherent vortical structure. In order to extract this specific spatial mode of pressure, a spatial box filtering (denoted as SBF hereinafter) is introduced in this study. A schematic diagram of SBF is shown in figure 7. As depicted in figure 7, 16 equally-spaced microphones, with uniform spacing $\Delta x/H = 0.5$, out of a whole 29-element array are used. The specific mode $\tilde{p}^{(i)}$, which corresponds to the spatial wavelength λ_i in the streamwise direction, is obtained by an inner product between the pressure distribution vector p_k and a spatial filter function $w_k^{(i)}$.

$$\tilde{p}^{(i)} = \sum_{k=0}^{N-1} p_k w_k^{(i)},$$

$$w_k^{(i)} = (-1)^{[k/2^{4-i}]}. \tag{4.1}$$

Here, p_k corresponds to the pressure at the kth sensor and N is the number of sensors. $[\cdot]$ represents a truncation to the nearest smaller integer. The waveform of $w_k^{(i)}$ is a square wave whose wavelength is $\lambda_i = 2^{4-i}H$. The SBF based on $w_k^{(i)}$ is a wavenumber

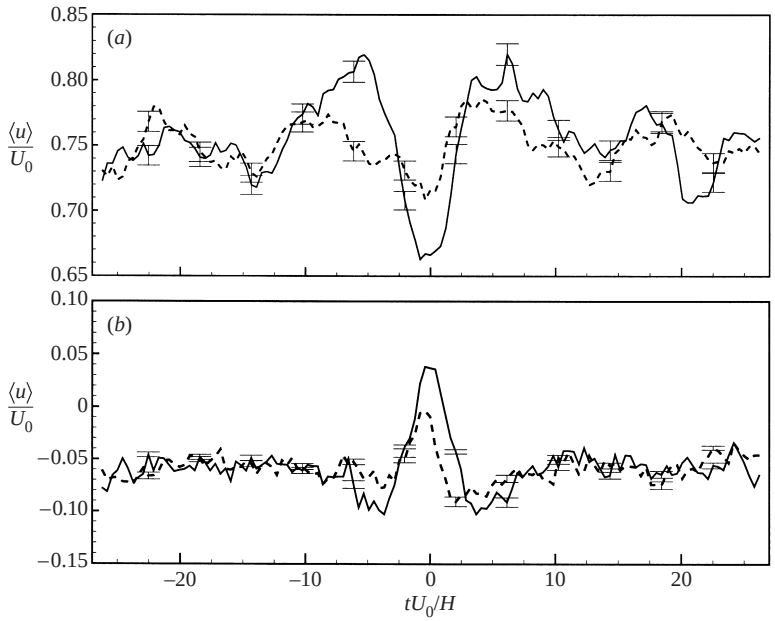

FIGURE 8. Comparison of the conditionally averaged velocity–time history measured at $x/H = 7.5$ and $y/H = 1.0$. —, conditional average based on the positive peak of $\tilde{p}^{(2)}$; - - -, based on the positive peak of p' at $x/H = 7.5$. (*a*) $\langle u \rangle / U_0$; (*b*) $\langle v \rangle / U_0$.

filtering tuned for a specific wavelength λ_i. As shown in figure 7, the wavelength of $w_k^{(2)}$ is $4H$, which is the length scale of a large-scale vortical structure. The SBF second mode of pressure $\tilde{p}^{(2)}$ represents the wavenumber components, which is pertinent to the large-scale vortical structure. On the other hand, the SBF zeroth mode of pressure $\tilde{p}^{(0)}$ pertains to global components of the entire measurement range including both the recirculation region and the reattaching region. The characteristics of $\tilde{p}^{(0)}$ will be explained later in § 5.

Based on the SBF second mode of pressure $\tilde{p}^{(2)}$, the conditionally averaged velocity–time histories $\langle u \rangle / U_0$ and $\langle v \rangle / U_0$ measured at $(x, y) = (7.5H, 1.0H)$ are displayed in figures 8(*a*) and 8(*b*), respectively. The conditional average based on the pressure fluctuations at $x/H = 7.5$ (denoted as p_R hereinafter) is also plotted by a dashed line for comparison. The zero non-dimensional time $tU_0/H = 0$ refers to the time instant when the two conditioning signals $\tilde{p}^{(2)}$ and p_R attain a peak over 2.5 times the r.m.s. level of each signal. Note that the conditional averages based on $\tilde{p}^{(2)}$ show larger velocity excursions than those associated with the local pressure peak. This implies that the randomness in the conditional average has been reduced by means of using an organized conditioning signal of $\tilde{p}^{(2)}$. The randomness stems from the 'improper' conditioning peaks in local pressure signals, which are uncorrelated with the coherent flow structures. The conditional averages in figure 8 show no appreciable information far from the zero time, say, $|tU_0/H| > 15$. This is attributed to the increasing uncertainties as the time difference increases. On the other hand, the conditionally averaged velocity excursions based on both signals almost coincide close to the zero time. The conditioning signal of $\tilde{p}^{(2)}$ appears to be in phase with the coherent component of p_R.

In order to look into the coincidence more closely, a comparison between the time histories of $\tilde{p}^{(2)}$ and p_R is made in figure 9. An example space–time plot of the

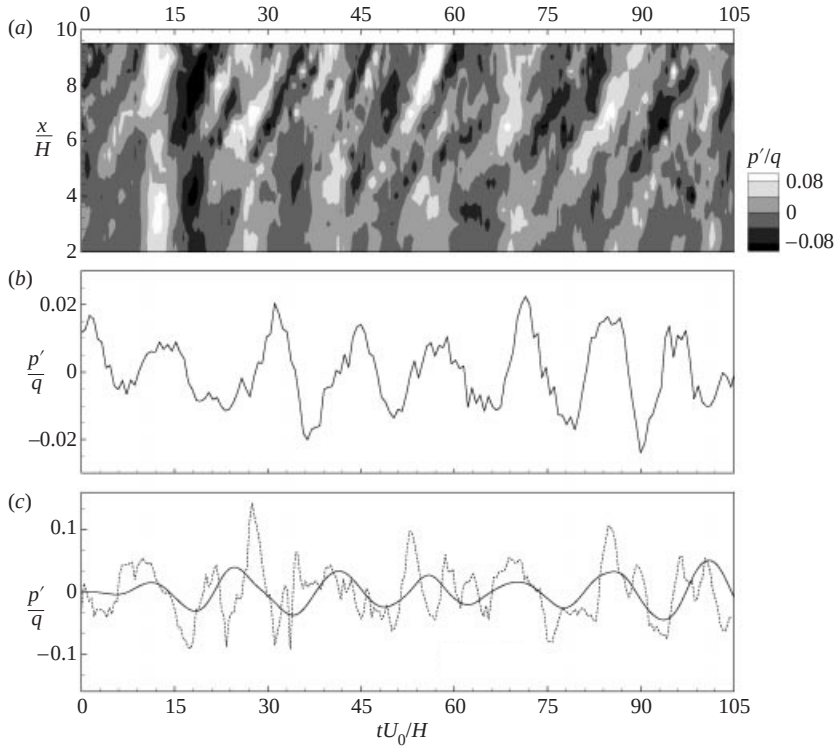

FIGURE 9. Example comparison of the spatial box filtered component and the shedding component. (*a*) Space–time contour plots of pressure fluctuations. (*b*) Time history of $\tilde{p}^{(2)}$ extracted from the space–time distribution of pressure fluctuations in (*a*). (*c*) Time history of the pressure fluctuations and the bandpass-filtered shedding component of pressure fluctuations at $x/H = 7.5$, with filtering in the range $0.05 \leqslant fH/U_0 \leqslant 0.08$. $\cdots$, unfiltered. —, shedding component.

pressure fluctuations is displayed in figure 9(*a*). The SBF second mode of pressure $\tilde{p}^{(2)}$ is calculated and then presented in figure 9(*b*). Figure 9(*c*) shows the time history of p_R extracted from figure 9(*a*). In addition, the coherent shedding component of p_R in figure 9(*c*) was obtained by bandpass filtering of the original signal for frequencies $0.05 \leqslant fH/U_0 \leqslant 0.08$. It is seen that $\tilde{p}^{(2)}$ in figure 9(*b*) attains a more regular periodicity compared to p_R in figure 9(*c*), while p_R shows some intermittent high-frequency fluctuations. As addressed in § 1, the high-frequency fluctuations are an artefact of the contributions from the irrelevant small-scale eddies. Furthermore, the oscillation magnitude of $\tilde{p}^{(2)}$ becomes larger in accordance with the 'vortex convection phase' in § 3.1, i.e. for $tU_0/H \sim 40$ and 75. This is attributable to the fact that the positive and negative packets of pressure fluctuations are scaled to nearly $2H$, which corresponds to the half-wavelength of $\tilde{p}^{(2)}$. This gives rise to a 'constructive interference' when applied to the spatial filtering. In addition, a closer comparison between $\tilde{p}^{(2)}$ and the filtered component of p_R indicates that they are almost the same in frequency and phase. In summary, $\tilde{p}^{(2)}$ provides a useful means for predicting a coherent eddy structure in separated and reattaching flows.

4.2. *Pressure–velocity correlation and conditionally averaged flow field*

In this section, the interrelation between $\tilde{p}^{(2)}$ and the whole flow field is examined in detail. The cross-correlation coefficient between the pressure $p(x_0, 0, t)$ at an arbitrary

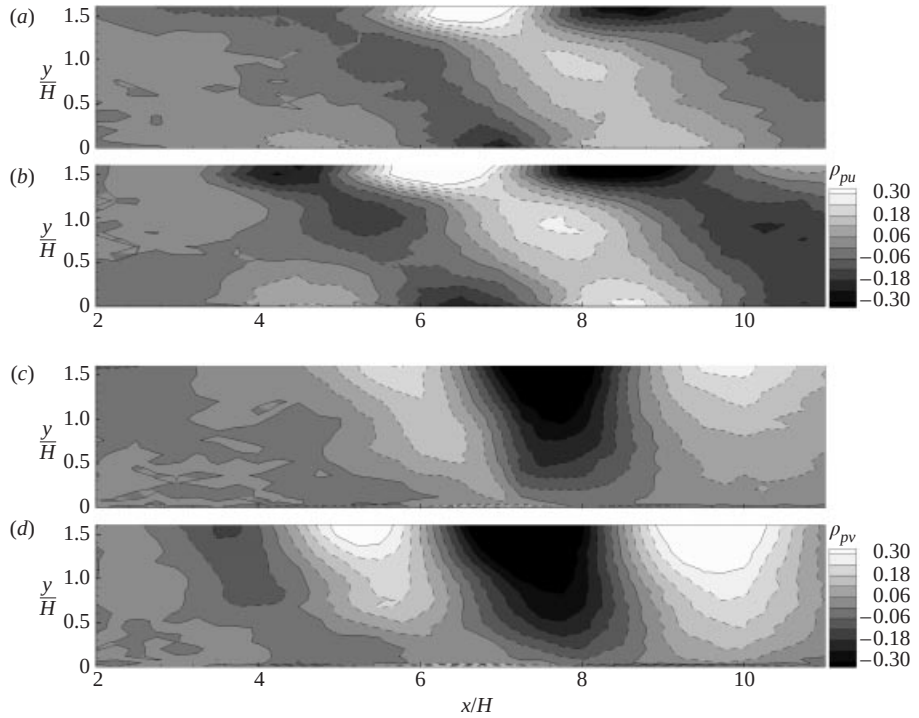

FIGURE 10. Comparison between p_R at $x/H = 7.5$ and $\tilde{p}^{(2)}$ in terms of the cross-correlation coefficient with velocity at zero time difference. Solid contour lines refers to zero correlation. (*a*) $\overline{p_R u}$; (*b*) $\overline{\tilde{p}^{(2)} u}$; (*c*) $\overline{p_R v}$; (*d*) $\overline{\tilde{p}^{(2)} v}$.

position and u-velocity field is defined as $\rho_{pu}(x, y, \tau) = \overline{p(x_0, 0, t)u(x, y, t + \tau)}/(p_{rms} u_{rms})$. By definition, the positive value of time difference τ indicates that the velocity field lags the pressure. In a similar manner, $\rho_{pv}(x, y, \tau)$ can be calculated. For simplicity, the notation $\overline{pv}$ will be used for the correlation coefficient instead of $\rho_{pv}(x, y, \tau)$. For the purpose of comparison, $p(x_0, 0, t)$ in the above equation is replaced by $\tilde{p}^{(2)}$ and p_R. The corresponding cross-correlation coefficients with zero time delay are illustrated in figure 10. A closer inspection of figures 10(*a*) and 10(*b*) discloses that $\overline{\tilde{p}^{(2)} u}$ is higher than $\overline{p_R u}$. Considering that $\tilde{p}^{(2)}$ is almost in phase with the shedding component of p_R, the two contour patterns are nearly the same. The same trend is observed between $\overline{p_R v}$ and $\overline{\tilde{p}^{(2)} v}$ in figures 10(*c*) and 10(*d*). The correlation enhancement by employing $\tilde{p}^{(2)}$ in the upstream region of the reattachment position, i.e. $4 \leqslant x/H \leqslant 7$ is explained as follows: as addressed in LS2, the vortical structure in the redeveloping region after reattachment is more organized than that in the recirculation region. The irregularity in the recirculation region is mainly attributed to the modulation from the flapping motion. In addition, the local pressure fluctuations are affected by the near wall small-scale eddies which are caused by the interaction between the large-scale shed vortices and the wall in the reattaching region. Thus, the employment of $\tilde{p}^{(2)}$, which is relatively unaffected by the above two kinds of irregularity, leads to the increase in the correlation level particularly in the recirculation region.

Sequential contour plots of the cross-correlation coefficient $\overline{\tilde{p}^{(2)} u}$ and $\overline{\tilde{p}^{(2)} v}$ with non-zero time difference are exhibited in figures 11 and 12. Five snapshots with time

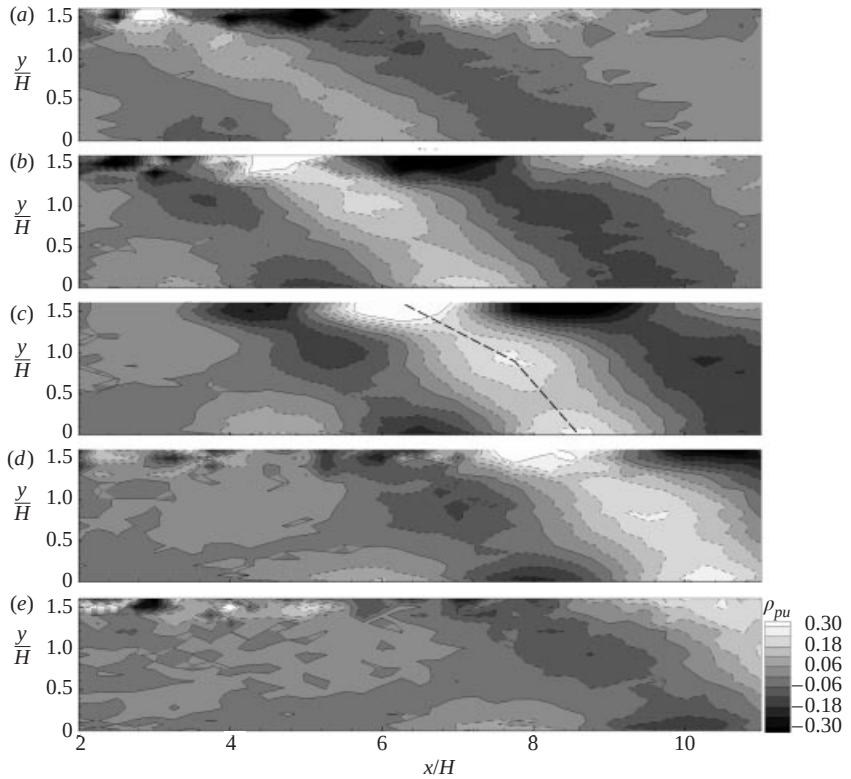

FIGURE 11. Sequential plots of the cross-correlation coefficient between the u-velocity and $\tilde{p}^{(2)}$ with respect to time differences τ. (*a*) $\tau = -\frac{1}{2}T$; (*b*) $\tau = -\frac{1}{4}T$; (*c*) $\tau = 0$; (*d*) $\tau = \frac{1}{4}T$; (*e*) $\tau = \frac{1}{2}T$.

differences $\tau = -\frac{1}{2}T$, $-\frac{1}{4}T$, 0, $\frac{1}{4}T$, $\frac{1}{2}T$ are displayed. Here, T represents the shedding period of large-scale vortices, $TU_0/H = 15.39$. The flow structures associated with the pressure fluctuations show a curved front convecting in the (x, y)-plane. In figure 11(*c*) with zero time difference, there exist three positive maxima of the correlation. The most dominant maximum at $(x, y) \sim (6.2H, 1.6H)$ suggests that the external irrotational flow is highly correlated with the wall pressure, which can be attributed again to the absence of incoherent velocity fluctuations caused by three-dimensional turbulent interactions (Kiya & Sasaki 1985). In fact, the extreme value of the pressure–velocity correlation in the region above the shear layer was pointed out by Cherry *et al.* (1984) (see their figures 34 and 35). Other maxima at $(7.68H, 0.94H)$ and $(8.58H, 0)$ are observed in figure 11(*c*) along with the virtual line segments connecting these three maxima. A closer inspection of figures 11(*b*) and 11(*c*) indicates that the originally straight 'correlation front' in figure 11(*b*) undergoes a deformation as it passes through the reattachment position. Thus, a retarding interaction between the reattaching eddy and the wall is suggested. The aforementioned correlation maxima at $(7.68H, 0.94H)$ and $(8.58H, 0)$ define an angle of 46° with the $-x$-axis. This angle is very close to the angle of 45° for the major axis of the vortical streamlines in the midspan plane of the hairpin vortices, which was observed by Kiya & Sasaki (1985). Furthermore, the abscissa of the maximum $(7.68H, 0.94H)$ corresponds to $0.13x_R$, which is comparable to the $0.18x_R$ in Kiya & Sasaki (1985). From the above results, this maximum can be regarded as a coherent vortex centre.

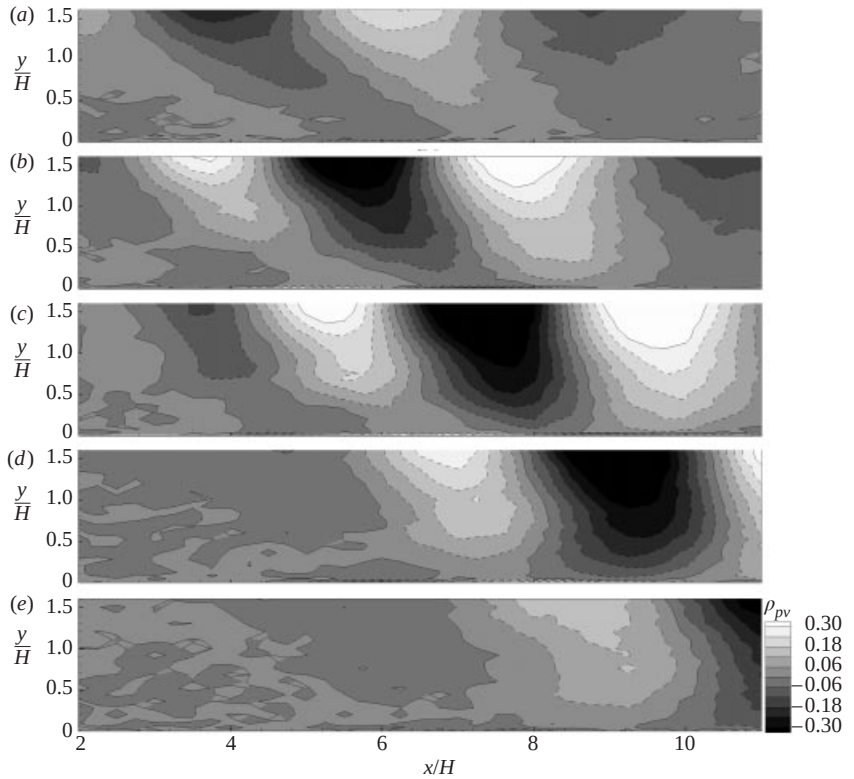

FIGURE 12. Sequential plots of the cross-correlation coefficient between the v-velocity and $\tilde{p}^{(2)}$ with respect to time differences τ. (*a*) $\tau = -\frac{1}{2}T$; (*b*) $\tau = -\frac{1}{4}T$; (*c*) $\tau = 0$; (*d*) $\tau = \frac{1}{4}T$; (*e*) $\tau = \frac{1}{2}T$.

The conditionally averaged vector fields $(\langle u\rangle, \langle v\rangle)$, synchronized with the negative and positive peaks of $\tilde{p}^{(2)}$, are plotted in figures 13(*a*) and 13(*c*), respectively. In all of the vector plots presented in this study, the convection velocity $U_c = 0.6U_0$ has been subtracted from $\langle u\rangle$ in order to delineate the vortical structure. In addition, the contours of vorticity ω, which is defined as $\omega \equiv \partial\langle u\rangle/\partial y - \partial\langle v\rangle/\partial x$, are also included in figures 13(*a*) and 13(*c*). The evolutionary energy distribution in the flow field can be analysed by means of the short time-averaged two-dimensional turbulence intensity k, which is a moving average of $\frac{1}{2}(u'^2 + v'^2)$ during one quarter of the shedding cycle $\frac{1}{4}T$. In figures 13(*b*) and 13(*d*), contours of the conditionally averaged turbulence intensity $\langle k\rangle/U_0^2$ are given in connection with the negative and positive peaks. Note that the ambiguity of the conditional average increases with the increasing time difference from the conditioning time references. Consequently, the results concerning both the negative and positive peaks have been obtained separately. From figures 13(*a*) and 13(*b*), the negative peak of $\tilde{p}^{(2)}$ is closely correlated with the passage of large-scale vortices near the reattachment point. An elliptical rotating shape is shown in the region $7 < x/H < 10$ of figure 13(*a*). This is identified as a vortical structure, because a maximum of the turbulence intensity appears in figure 13 near the centre of the rotating system at $(x, y) \sim (8.0H, 1.0H)$. On the contrary, when $\tilde{p}^{(2)}$ attains a positive peak (figures 13*c* and 13*d*), an engulfment of the shear layer toward the wall near $x/H = 8$ is observed. The neck of the high-turbulence-intensity region near $x/H = 7.5$ may be caused by the down-

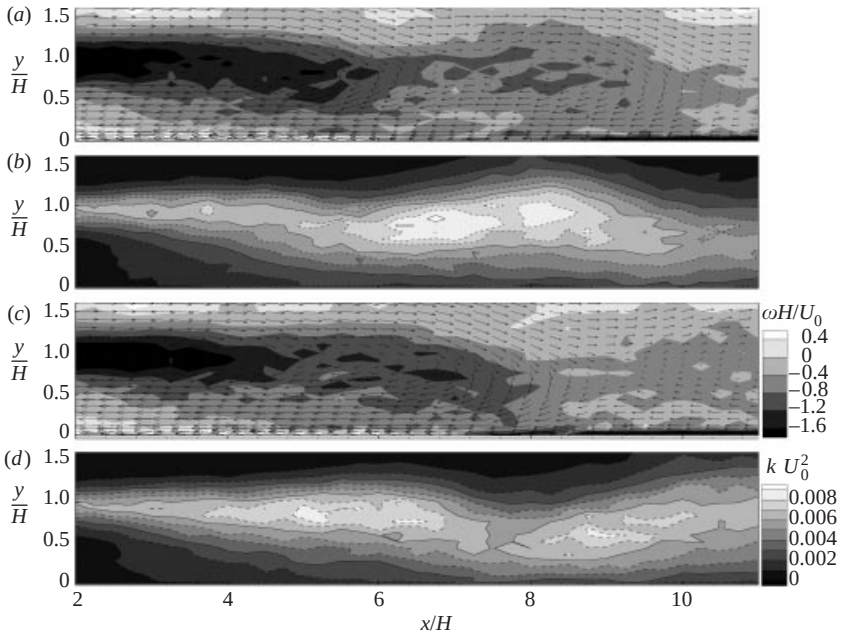

FIGURE 13. Conditionally averaged vector plot and contour plots of vorticity and turbulence intensity. (*a*) Vector plot and contour plot of vorticity and (*b*) contour plot of turbulence intensity, which coincides with the negative peak of $\tilde{p}^{(2)}$. (*c*) and (*d*) are synchronized with the positive peak. The convection velocity of $0.6U_0$ has been subtracted from the conditionally averaged streamwise velocity.

wash of the external irrotational flow, which is entrained by the upstream vortical structure located at $x/H = 6.0$. In addition, the previously shed vortex is found near $x/H = 10$. These observations are in close agreement with those in Kiya & Sasaki (1985). Furthermore, the intensity contour of figure 13(*d*) implies that the vortical structure is elongated along the streamwise direction after reattachment. These are closely consistent with the spanwise vorticity contours in Le, Moin & Kim (1997).

Sequential plots of the conditionally averaged vector field and the vorticity contours pertaining to the negative peak of $\tilde{p}^{(2)}$ are shown in figure 14 during one shedding cycle. The time differences are the same as those in figure 11. The corresponding sequential contour plots of the turbulence intensity are presented in figure 15. The vector plots in figures 14(*a*) and 14(*e*), which are one shedding cycle apart from each other, appear to be almost the same. This is in support of the periodicity of the vortex shedding. These instances are 180° out of phase with the negative peak in terms of the shedding period so that they correspond to the positive peaks. The extended high-vorticity region along the shear layer up to $x/H \sim 7$ is exactly the same as that in figure 13(*c*). However, the saddle point of the vector field is not identified, whereas it could be found in the middle of two vortices in figure 13(*c*). The instances of figures 14(*a*) and 14(*e*) are more or less deviated from the conditioning peaks so that a certain amount of randomness is included in the estimation of the velocity vector field. After a quarter period from figure 14(*a*), a newly formed vortical structure near $x/H = 6$ begins to be shed in figure 14(*b*). This vortical structure is completely detached from the upstream shear layer in figure 13(*c*), and then it convects downstream as far as $x/H \sim 10$ in figure 14(*d*).

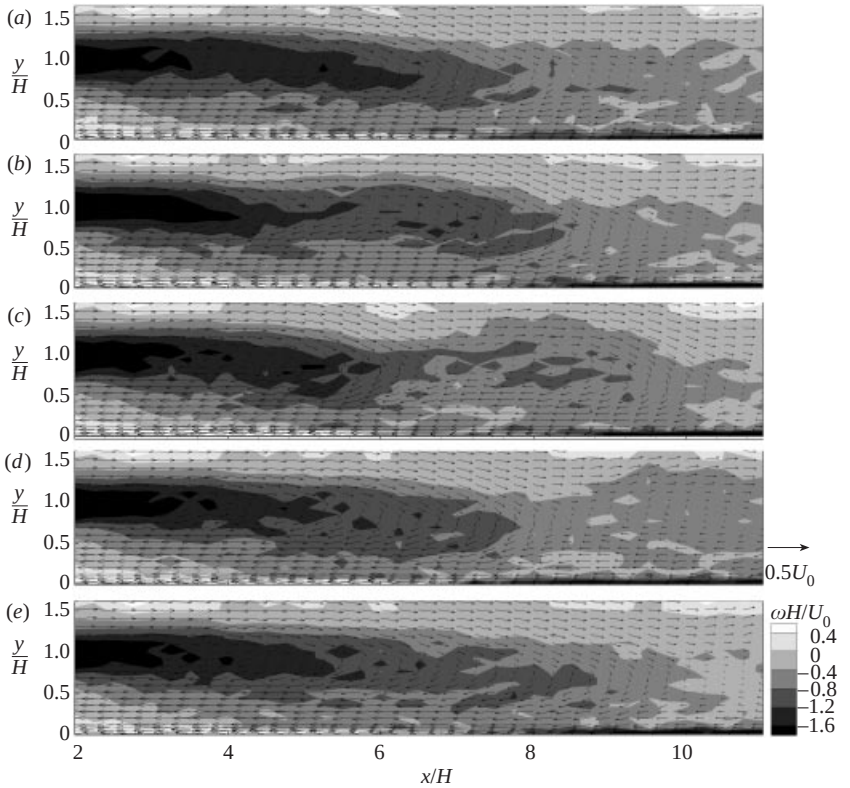

FIGURE 14. Sequential plots of the conditionally averaged vector plot and contour plot of vorticity based on the negative peak of $\tilde{p}^{(2)}$. (*a*) $t = -\frac{1}{2}T$; (*b*) $t = -\frac{1}{4}T$; (*c*) $t = 0$; (*d*) $t = \frac{1}{4}T$; (*e*) $t = \frac{1}{2}T$.

The formation and convection of the vortical structure are similar to those observed in figure 15, where the vortex core travels about $4H$ during $\frac{1}{2}T = 7.69H/U_0$. This gives an estimated convection velocity of $0.52U_0$, which is slightly smaller than the $0.6U_0$ obtained in LS1 from the analysis of the frequency–wavenumber spectrum.

Space–time contours of the conditionally averaged streamwise velocity measured at $y/H = 0.04$ are shown in figures 16(*a*) and 16(*b*), based on the negative and positive peaks of $\tilde{p}^{(2)}$. Note that unsteadiness of the reattaching region is well elucidated by these spatio-temporal maps of the surface velocity. The solid contour line corresponds to the zero instantaneous streamwise velocity, i.e. a trace of the instantaneous reattachment position. A so-called sawtooth shape is displayed in figure 16(*a*), where the reattachment position retreats all at once with the passage of large-scale vortices at $tU_0/H \sim 0$ after a gradual advancement. This is in close agreement with the spanwise-averaged reattachment position by Le *et al.* (1997). In addition, Kiya & Sasaki (1985) showed a similar movement of the reattachment point from the conditional average of velocity–time history. The scenario of this sawtooth movement proposed by Le *et al.* (1997) is that the reattachment position travels downstream with a constant speed along with the growth of the large-scale vortical structure and then goes back abruptly with the detachment of the vortical structure from the shear layer. This situation is found to reappear in figures 13–16.

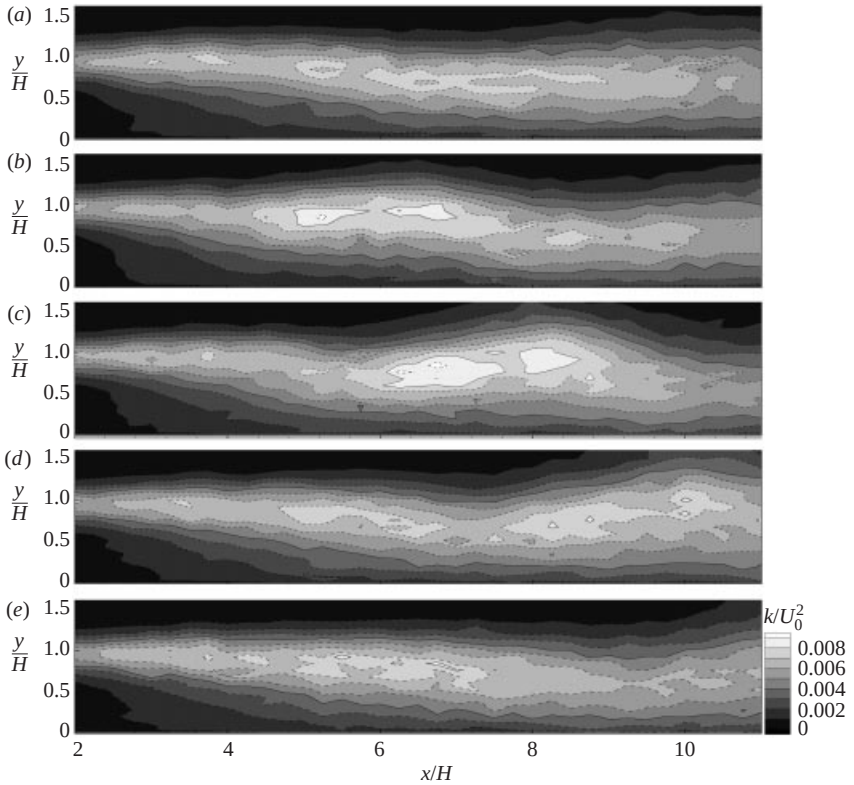

FIGURE 15. Sequential plots of the conditionally averaged contour plot of turbulence intensity based on the negative peak of $\tilde{p}^{(2)}$. (*a*) $t = -\frac{1}{2}T$; (*b*) $t = -\frac{1}{4}T$; (*c*) $t = 0$; (*d*) $t = \frac{1}{4}T$; (*e*) $t = \frac{1}{2}T$.

5. Features of the flapping motion

Whereas the preceding section was devoted to the analysis of large-scale vortical structures based on $\tilde{p}^{(2)}$, the unsteady aspects of the flapping motion are scrutinized in this section. Toward this end, the lowpass-filtered pressure and the SBF zeroth mode of pressure $\tilde{p}^{(0)}$ are employed. In a manner similar to figure 9, figure 17 illustrates an example comparison of these time histories. A space–time contour plot of the pressure fluctuations is represented in figure 17(*a*) to accommodate the global oscillation phase near $tU_0/H \sim 10$ and 155. The time history of $\tilde{p}^{(0)}$ is displayed in figure 17(*b*). Since the global oscillation phase is indicative of the time instant when the pressure fluctuations show entirely in-phase oscillations, the uniform shape of $w_k^{(0)}$ in figure 7 renders $\tilde{p}^{(0)}$ to attain a maximum amplitude. Time histories of the lowpass-filtered pressure fluctuations at $x/H = 2.0$, 4.0 and 7.5 are shown in figure 17(*c*). The cutoff frequency of the lowpass filter is $fH/U_0 = 0.015$. As pointed out by the wavelet analysis in § 3.2, the flapping component of the pressure fluctuations is considered as a standing wave. Three time histories of the pressure fluctuations in figure 17(*c*) show an overall agreement. Moreover, a comparison between figures 17(*b*) and 17(*c*) indicates that the global oscillation occurs when the flapping component increases from negative to positive value.

In order to further examine the relation between the flapping motion and $\tilde{p}^{(0)}$ in the frequency domain, the coherence between $\tilde{p}^{(0)}$ and the *u*- and *v*-velocity fields, denoted by Γ_{pu} and Γ_{pv}, is plotted in figure 18. It is seen that Γ_{pu} in figure 18(*a*) shows a high

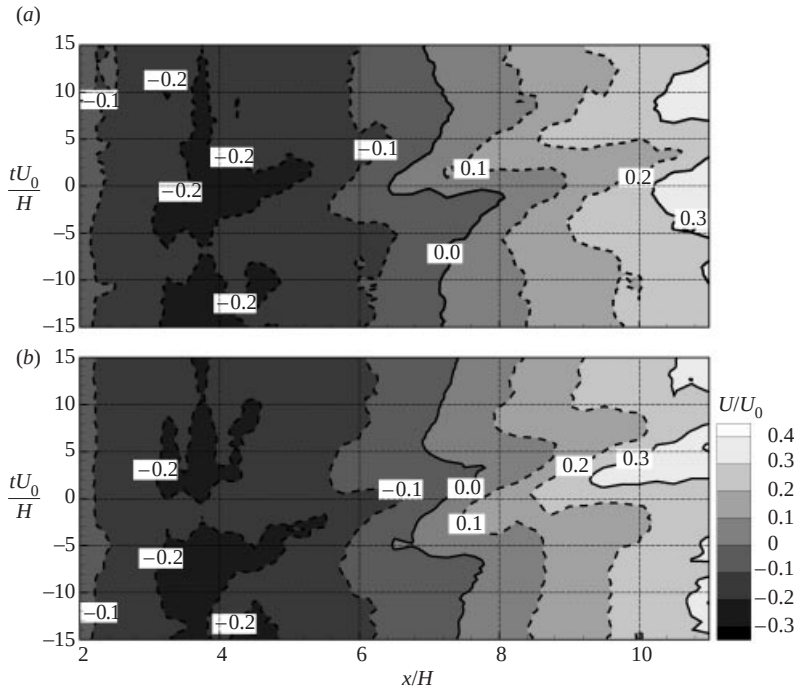

FIGURE 16. Contour plots of conditionally averaged surface u-velocity at $y/H = 0.04$. Synchronization time in (a) and (b) corresponds to the negative and the positive peak of $\tilde{p}^{(2)}$, respectively.

level of coherence near the low-frequency end in the region $2 < x/H < 7$, together with the frequency of the large-scale vortical structure. The coherence between $\tilde{p}^{(2)}$ and the u-velocity field (not shown here for brevity) might be obtained in a similar manner. However, this does not show any appreciable values in the flapping frequency range. In § 3.2, it is postulated that the enlargement (shrinkage) of the recirculation region is associated with the positiveness (negativeness) of the lowpass-filtered flapping component of pressure fluctuations. Since the magnitude of the flapping component of pressure fluctuations is much smaller than that of the unfiltered pressure, it is difficult to find the enlargement/shrinkage mechanism in terms of $\tilde{p}^{(0)}$. Thus, $\tilde{p}^{(0)}$ is used as a conditioning signal for the global oscillation phase only. Instead, the enlargement/shrinkage process will be observed by means of the lowpass-filtered component of pressure fluctuations at $x/H = 7.5$, denoted as p_F.

In figure 19, contour plots of the stream function obtained from the conditionally averaged velocity field are presented. These coincide with the negative/positive peaks of p_F and the negative peak of $\tilde{p}^{(0)}$. Since the large positive and negative fluctuations of $\tilde{p}^{(0)}$ occur in a short time interval of the global oscillation phase, the positive peak has not been dealt with here. For the negative peak of p_F in figure 19(a), the streamlines of the shear layer at $(x, y) \sim (8H, 1H)$ show a slight concave curvature compared to those in figure 19(b). In addition, the dashed streamlines of the recirculation region in figure 19(b) are extended further downstream than those in figure 19(a). These observations are in support of the above assumption of the relationship between the polarity of p_F and the enlargement/shrinkage of the recirculation region. For the global oscillation phase given in figure 19(c), the recirculation region is retracted

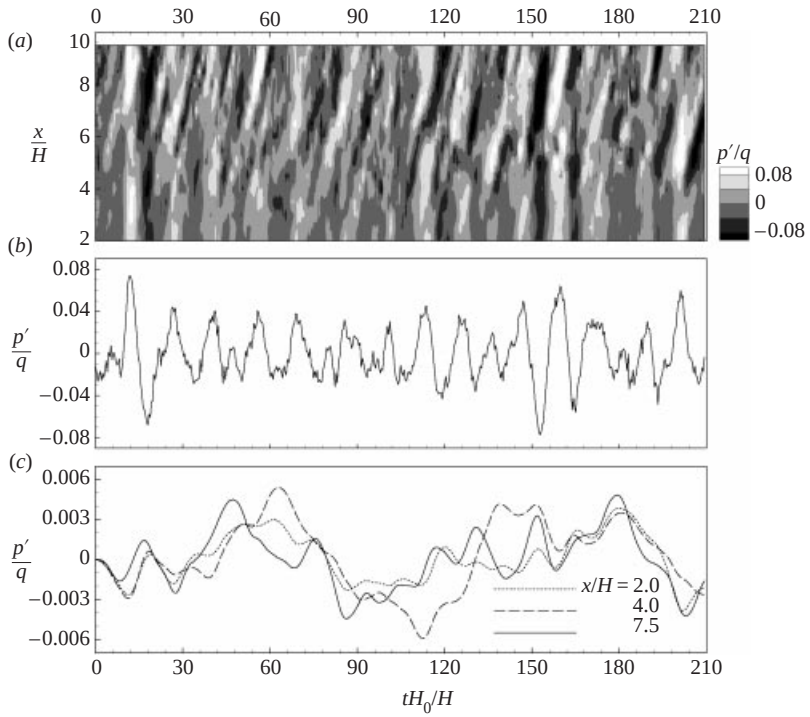

FIGURE 17. Example comparison of the spatial box filtered component and the flapping component. (*a*) Space–time contour plots of pressure fluctuations. (*b*) Time history of $\tilde{p}^{(0)}$ extracted from the space–time distribution of pressure fluctuations in (*a*). (*c*) Time history of the pressure fluctuations and the lowpass-filtered flapping component of pressure fluctuations at $x/H = 2.0$, 4.0 and 7.5, with cutoff frequency $fH/U_0 = 0.015$.

toward the most upstream position. In addition, the strength of the reverse flow is higher than that in figure 19(*a*).

Space–time contours of the stream functions, which are obtained along $y/H = 1.0$, are represented in figure 20 with the same time references as those in figure 19. The results are consistent with those in figure 19; first, the negative p_F in figure 20(*a*) and the positive p_F in figure 20(*b*) are correlated with the shrinkage and enlargement motion of the recirculation region, respectively. Secondly, the oscillatory behaviour in figure 20(*c*) suggests that the global oscillation is an up–down vibratory behaviour of the shear layer. In the vicinity of the wall, the same relationship between p_F and the shrinkage/enlargement process can be seen in figures 21(*a*) and 21(*b*). Spatio-temporal behaviours of the reattachment position owing to the flapping motion are represented in figure 21. The conditional averages are based on the lowpass-filtered component pressure p_F. Accordingly, the features of the convection of large-scale vortical structure in figure 16 are supposed to decay out from the 'mismatched' time references of the present conditional averaging scheme.

The above results regarding the flapping motion can be summarized in a schematic diagram, as shown in figure 22. Originally, this schematic diagram was shown in LS2, but a major modification has been made based on the unsteady flow field features due to the flapping motion in the present study. The shrinkage, global oscillation and enlargement are denoted along with the progress of time. Since the global oscillation phase is accompanied by the increasing zero of p_F, this state is considered to take

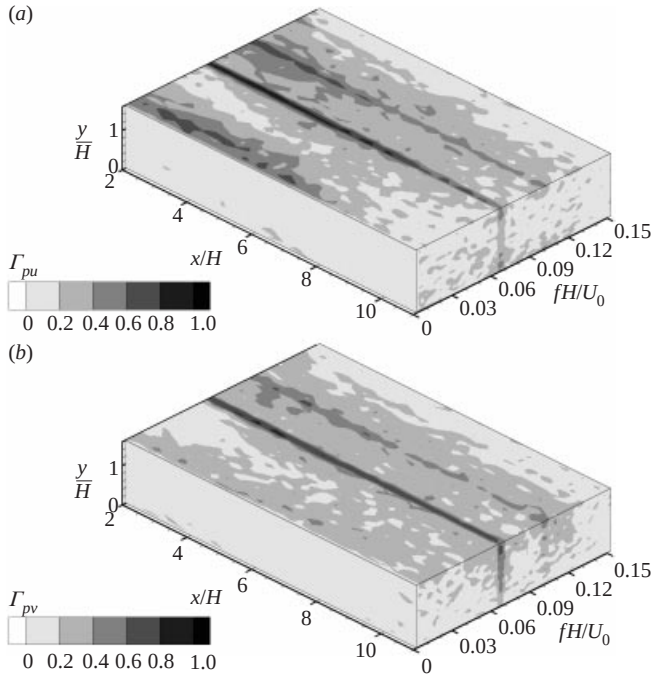

FIGURE 18. Coherence between the velocity and $\tilde{p}^{(0)}$. (*a*) Γ_{pu}; (*b*) Γ_{pv}.

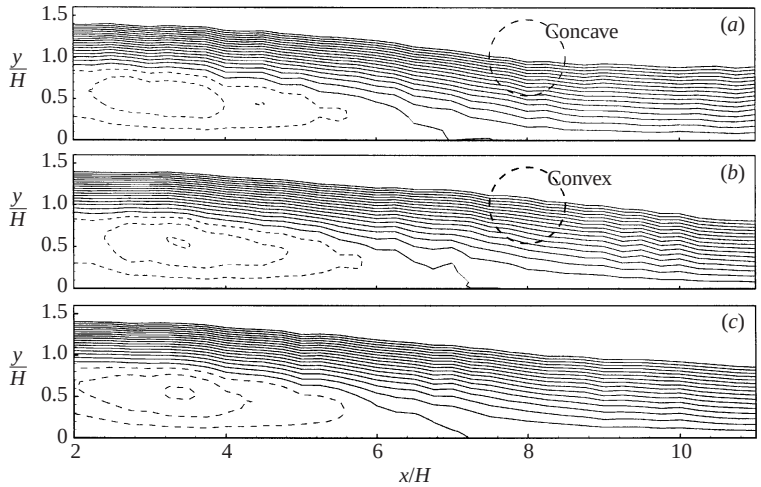

FIGURE 19. Contour plots of conditionally averaged stream function with respect to the (x, y)-plane. Contour levels are from −0.1 to 0.4 with a step of 0.25 with the dashed contours corresponding to negative value. (*a*) Negative peak of the flapping component of pressure at $x/H = 7.5$; (*b*) positive peak of the flapping component of pressure at $x/H = 7.5$; (*c*) negative peak of $\tilde{p}^{(0)}$, respectively.

place in the final stage of the shrinkage state of the recirculation region owing to the flapping motion. Considering the merging of pressure contours denoted at figures 5(*a*) and 5(*b*), it seems reasonable to state that the global oscillation phase occurs when the downstream convection of the vortical structure is decelerated by the contraction of the recirculation region. Accordingly, one vortical structure is caught up with the

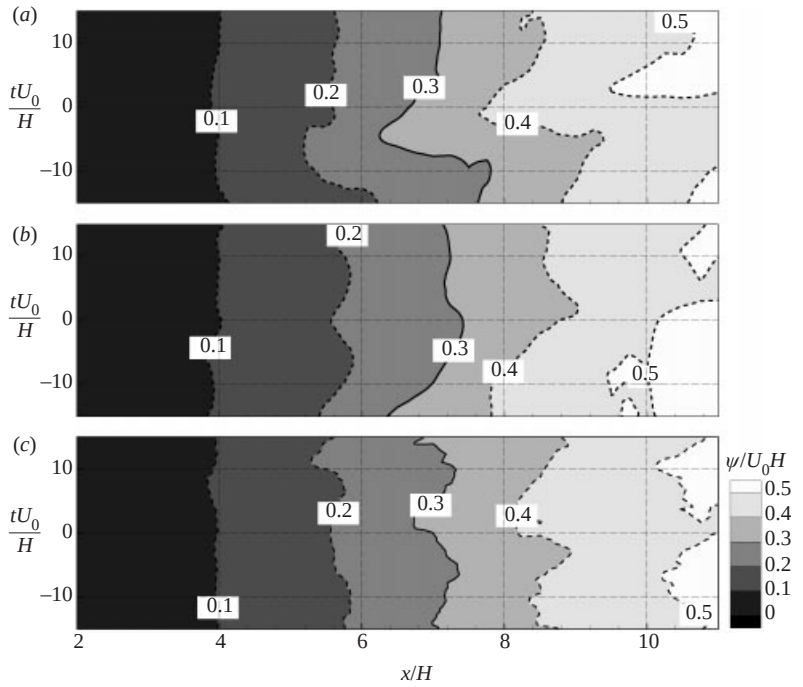

FIGURE 20. Contour plots of conditionally averaged stream function measured at $y/H = 1.0$.

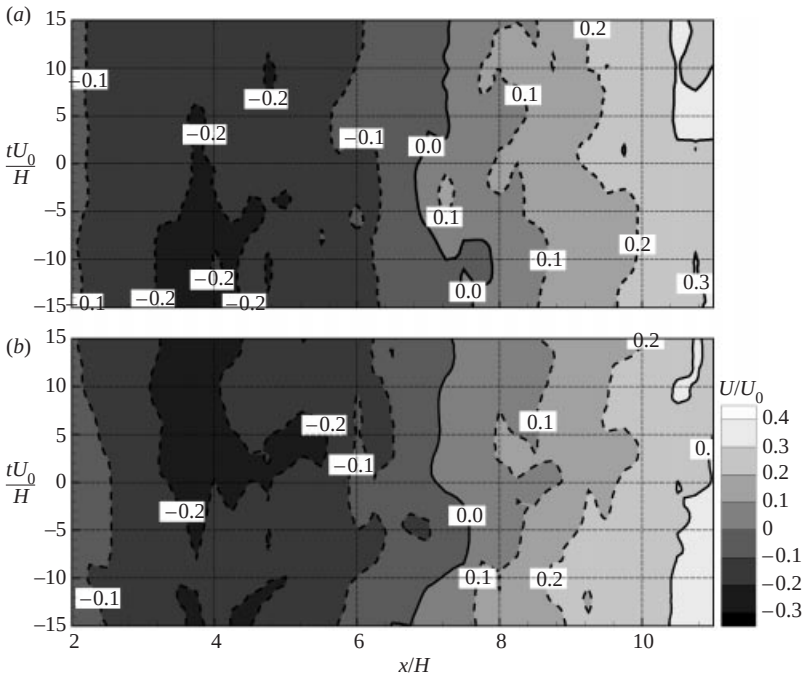

FIGURE 21. Contour plots of conditionally averaged surface u-velocity measured at $y/H = 0.04$.

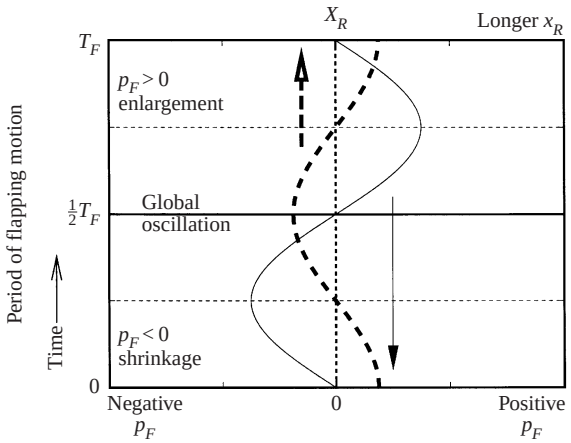

FIGURE 22. Time relationship between p_F and the movement of x_R due to flapping motion. —, p_F; - - -, x_R due to flapping motion.

next one. It is worth mentioning that the flapping motion is considered as a periodic movement in figure 22. This is contrary to the assumption of Eaton & Johnston (1982), who regarded an unusual event as the cause of the short-term breakdown of the spanwise vortices and the consequent inflation of the recirculation region. In fact, the consistency found in the present results by means of the conditional average would not exist without a periodicity of the flapping motion. Therefore, as mentioned by Kiya & Sasaki (1985), some feedback mechanism inside a whole separation bubble is believed to exist.

6. Concluding remarks

Unsteady characteristics of wall pressure fluctuations in the separated and reattaching flows over a backward-facing step and their relationship with relevant flow modes have been described by means of a variety of signal processing methods. The wavelet analysis of pressure–time histories from an array of microphones elucidated various evolutionary features of the flow field which are closely associated with the large-scale vortical structure and the flapping motion. From these results, a scenario pertaining to the modulation of the vortical structure caused by the flapping motion was then postulated. In the present account, which is a sequel to Lee & Sung (2001*a*) and Lee & Sung (2001*b*), the pressure–velocity joint measurement has been performed on a centreplane in a flow over a backward-facing step. Every single velocity measurement was accompanied by the measurement of pressure spatial distribution with respect to the streamwise direction. From the space–time information of the pressure fluctuations, an effective means to extract a relevant spatial mode due to the large-scale vortical structure has been introduced and discussed. This is termed as 'spatial box filtering (SBF)' with a specific discrete ith mode whose spatial wavelength is equal to $2^{4-i}H$. Emphasis is placed on the SBF second mode of pressure $\tilde{p}^{(2)}$ with the wavelength corresponding to the length scale of the large-scale vortical structure. This mode then turns out to be well correlated with the flow field of the vortical structure. This result provides evidence that the pressure fluctuations are mainly due to the vortical structure in the shear layer. Regarding the modulated behaviour of coherent structure by the flapping motion, the relation between the lowpass-filtered pressure and the periodic shrinkage/enlargement motion of the separation bubble

has been established. It should be pointed out that there are still unsolved questions regarding more detailed three-dimensional flow structure and the feedback mechanism of the flapping motion. Toward this end, more extensive measurement capacity must be required, e.g. a two-dimensionally arranged microphone array with respect to the spanwise direction as well as the streamwise direction. A more elaborate experimental study based on this measurement facility would be a good subject for future work. Finally, what is worth emphasizing here is that an instrumentation methodology for the prediction of dynamic behaviour of the reattaching shear layer has now been successfully furnished with a feasible measurement and signal processing capability in the present account.

This work was supported by a grant from the National Research Laboratory of the Ministry of Science and Technology, Korea.

REFERENCES

Addison, P. S. 1999 Wavelet analysis of the breakdown of a pulsed vortex flow. *Proc. Inst. Mech. Engrs* C **213**, 217–229.

de Brederode, V. & Bradshaw, P. 1978 Influence of the side walls on the turbulent centerplane boundary-layer in a squareduct. *Trans. ASME* I: *J. Fluids Engng* **100**, 91–96.

Cherry, N. J., Hillier, R. & Latour, M. E. M. P. 1984 Unsteady measurements in a separated and reattaching flow. *J. Fluid Mech.* **144**, 13–46.

Chun, K. B. & Sung, H. J. 1996 Control of turbulent separated flow over a backward-facing step. *Exps. Fluids* **21**, 417–426.

Devenport, W. J. & Sutton, E. P. 1991 Near-wall behavior of separated and reattaching flows. *AIAA J.* **29**, 25–31.

Driver, D. M., Seegmiller, H. L. & Marvin, J. G. 1987 Time-dependent behavior of a reattaching shear layer. *AIAA J.* **25**, 914–919.

Eaton, J. K. & Johnston, J. P. 1981 A review of research on subsonic turbulent flow reattachment. *AIAA J.* **19**, 1093–1100.

Eaton, J. K. & Johnston, J. P. 1982 Low frequency unsteadiness of a reattaching turbulent shear layer. In *Turbulent Shear Flows*, vol. 3, pp. 162–170.

Farge, M. 1992 Wavelet transforms and their application to turbulence. *Annu. Rev. Fluid Mech.* **24**, 395–437.

Heenan, A. F. & Morrison, J. F. 1998 Passive control of pressure fluctuations generated by separated flow. *AIAA J.* **36**, 1014–1022.

Hijikata, K., Suzuki, Y. & Iwana, K. 1996 Flow visualization by velocity-pressure cross correlation. *Trans. ASME* I: *J. Fluids Engng* **118**, 486–493.

Johansson, A. V., Her, J. Y. & Haritonidis, J. H. 1987 On the generation of high-amplitude wall-pressure peaks in turbulent boundary layers and spots. *J. Fluid Mech.* **175**, 119–142.

Kiya, M. & Sasaki, K. 1985 Structure of large-scale vortices and unsteady reverse flow in the reattaching zone of a turbulent separation bubble. *J. Fluid Mech.* **154**, 463–491.

Le, H., Moin, P. & Kim, J. 1997 Direct numerical simulation of turbulent flow over a backward-facing step. *J. Fluid Mech.* **330**, 349–374.

Lee, I. & Sung, H. J. 2001*a* Characteristics of wall pressure fluctuations in separated flows over a backward-facing step. Part I Time-mean statistics and cross-spectral analyses. *Exps. Fluids* **30**, 262–272.

Lee, I. & Sung, H. J. 2001*b* Characteristics of wall pressure fluctuations in separated flows over a backward-facing step. Part II Unsteady wavelet analysis. *Exps. Fluids* **30**, 273–282.

Mabey, D. G. 1972 Analysis and correlation of data on pressure fluctuations in separated flow. *J. Aircraft* **9**, 642–645.

Poggie, J. & Smits, A. J. 1997 Wavelet analysis of wall-pressure fluctuations in a supersonic blunt-fin flow. *AIAA J.* **35**, 1597–1603.

Ra, S. H., Chang, P. K. & Park, S. O. 1990 A modified calibration technique for the split film sensor. *Meas. Sci. Tech.* **1**, 1156–1161.